

Helical Ribbons: Simple Chiral Sedimentation

Elias Huseby,¹ Josephine Gissinger,² Fabien Candelier,² Nimish Pujara,³ Gautier Verhille,⁴ Bernhard Mehlig,⁵ and Greg Voth^{1,*}

¹*Department of Physics, Wesleyan University, Middletown, CT 06459, USA*

²*CNRS, IUSTI, Aix Marseille University, Marseille, France*

³*Department of Civil and Environmental Engineering,*

University of Wisconsin-Madison, Madison, WI 53706 USA

⁴*Aix Marseille Univ. CNRS, Centrale Marseille, IRPHE, F-13384 Marseille, France*

⁵*Department of Physics, Gothenburg University, 41296 Gothenburg, Sweden*

We investigate the sedimentation of chiral particles in viscous fluid flow. We identify helical ribbons as simple particles with strong translation-rotation coupling whose symmetry ensures that the centers of mass, buoyancy, resistance, and mobility coincide. Experimental measurements of both relevant mobility tensors show excellent agreement with simulations of ribbons made of interacting spheres. We observe quasi-periodic angular dynamics causing complex spatial trajectories. In tilt-spin phase space, orbits are closed due to time-reversal and reflection symmetry. Changing the helical ribbon length reveals a bifurcation at which the stable sedimentation orientations switch.

How can the geometry of a rigid solid particle be used to manipulate its sedimentation through a highly viscous fluid? This has been a central problem in fluid dynamics and there are many pressing applications such as the transport of plankton [1] or microplastics [2].

The underlying Stokes flow theory is well known [3–5], but analytic or numerical predictions for the mobility or resistance tensors that are validated by experimental measurements are rare, particularly for particles that couple translation to rotation [6–10].

In the viscous limit, and with no velocity gradients in the fluid, particle velocity \mathbf{v} and rotation rate $\boldsymbol{\omega}$ depend linearly on externally applied force \mathbf{f} and torque $\boldsymbol{\tau}$:

$$\begin{bmatrix} \mathbf{v} \\ \boldsymbol{\omega} \end{bmatrix} = \frac{1}{\mu} \begin{bmatrix} \mathfrak{a}' & \mathfrak{b}'^T \\ \mathfrak{b}' & \mathfrak{c}' \end{bmatrix} \begin{bmatrix} \mathbf{f} \\ \boldsymbol{\tau} \end{bmatrix} \quad (1)$$

The mobility tensors \mathfrak{a}' , \mathfrak{b}' , and \mathfrak{c}' are determined by particle shape and orientation [3], with primes indicating that these are in the laboratory frame. In sedimentation problems for particles with homogeneous mass density, the torque can be computed about the common center of mass and buoyancy which sets $\boldsymbol{\tau}$ to zero. Then with the rotation matrix from the body-fixed frame to the lab frame, \mathbb{R} , the equations of motion are

$$\frac{d}{dt} \mathbf{x} = \mathbf{v}, \quad \mu \mathbf{v} = \mathbb{R} \mathfrak{a} \mathbb{R}^{-1} \mathbf{f} \quad (2a)$$

$$\frac{d}{dt} \mathbb{R} = \boldsymbol{\omega} \wedge \mathbb{R}, \quad \mu \boldsymbol{\omega} = \mathbb{R} \mathfrak{b} \mathbb{R}^{-1} \mathbf{f}. \quad (2b)$$

A core difficulty of this problem is the strongly non-linear relationship between particle geometry and mobility tensors. Recent advances in fabrication and tracking have allowed experimental measurements of particles with complex geometries and the observed dynamics have been quite surprising. Collins *et al.* [8] showed that the isotropic helicoid proposed by Kelvin in 1871 [11] has much smaller translation-rotation coupling than expected [3, 12]. Miara *et al.* [9] identified a particle that

is non-chiral and yet exhibits translation-rotation coupling with chiral trajectories whose handedness depends on initial particle orientation.

Many different applications have motivated theoretical work connecting particle geometry and sedimentation dynamics [13–17]. Witten and Diamant [5] review the wide range of possible dynamics of chiral sedimentation. Particles typically have periodic orbits in orientation when \mathfrak{b} is symmetric while approaching fixed orientations when there is an anti-symmetric part of \mathfrak{b} [14, 17]. The consequences of shape symmetries for particle dynamics have been explored in some detail [5, 8, 15, 18–21], but there still does not exist a general framework for classifying particle trajectories based on shape, or for guiding design of particle shapes with desired trajectories.

In this paper, we identify an underlying reason why new particle shapes continue to surprise us. We do not have a clear roadmap that leads from shapes with simpler \mathfrak{b} tensors through more complex geometries. For the \mathfrak{a} tensor, the roadmap from spheres through spheroids to triaxial ellipsoids already spans all possibilities since \mathfrak{a} is symmetric and so is diagonal in its eigenbasis. If we define torques using the center of mobility (also called center of twist [5]) then \mathfrak{b} is also symmetric. So when the center of mass, buoyancy, and mobility coincide, \mathfrak{b} is symmetric around a point with zero torque. Additionally, if \mathfrak{a} , \mathfrak{b} , and \mathfrak{c} are all diagonal in the same eigenbasis, then the center of resistance is equal to the center of mobility [4]. Co-centered particles with a single center of mass, buoyancy, resistance, and mobility are a natural simplest case for particles with non-trivial \mathfrak{b} tensors.

The chiral particles that have received the most attention in the literature are not co-centered. The importance of bacterial flagella led Purcell [6] and a sequence of researchers [10, 16, 22, 23] to focus on helical fibers. These are efficient at propulsion and accessible to theory and computation through slender body theory. However, for arbitrary lengths, they are not co-centered. Experimen-

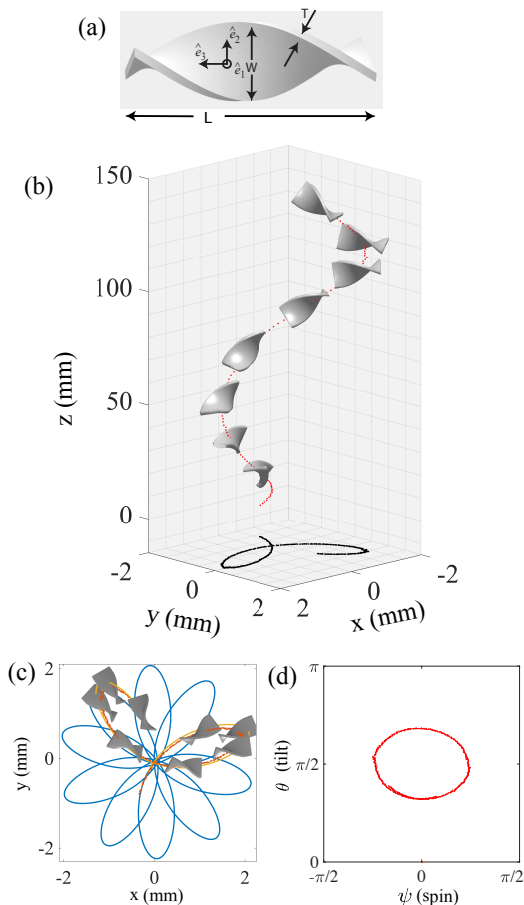


FIG. 1. (a) Body coordinate system and dimensions for a helical ribbon with Length $2\pi L/s = 5\pi/4$ (b) A measured trajectory in space (Helix is not to scale, length $3\pi/4$) (c) top view. Red dots are measurements. Yellow line is a numerical integration using measured parameters for this particle. Blue line continues the numerical trajectory. (d) Same measured trajectory in tilt-spin space. Supplemental video is available [24].

tal measurements of translation-rotation coupling of helical fibers find good agreement with predictions, but have only explored a single tensor element along the axis [23].

We study helical ribbons, formed by a thin rectangular sheet twisted about its long axis so that its long edges form a double helix, shown in Fig. 1(a). These particles are co-centered because they have three perpendicular axes with discrete symmetry under rotation by π . Two of these symmetries are sufficient to ensure that a particle is co-centered since any rotational symmetry fixes all centers to lie along the rotation axis.

We fabricated helical ribbons using projection micro stereolithography 3D printing in order to obtain precise geometry and good density homogeneity [24]. Four different helical ribbons were used with different lengths labeled by their twist angles, $2\pi L/s = 3\pi/4$, $5\pi/4$, $4\pi/3$, and $3\pi/2$, where $s = 20$ mm is the length over which

the helix twists through a full rotation. All particles had width $W=4$ mm, thickness $T = 0.5$ mm, and density 1.20 g/cm³. They were dropped in a 20x20x20 cm tank of silicon oil with mass density $\rho = 0.97$ g/cm³ and kinematic viscosity $\mu/\rho = 520$ cSt. The particle Reynolds number based on length, $Re_p = L|\mathbf{v}|/\mu$, ranged between $0.027 < Re_p < 0.092$, firmly in the viscous limit.

Three-dimensional positions and orientations of particles were reconstructed using 3 cameras with nearly orthogonal viewing angles [24, 25]. It is convenient to measure particle orientation using Euler angles [26] where ψ measures spin about the particle's long axis, θ is the polar angle measuring the tilt of body coordinate \hat{e}_3 away from vertical, and ϕ is the azimuthal angle. We define $\psi = 0$ to be when \hat{e}_1 is normal to the plane formed by \hat{e}_3 and the z axis. Note that tilts away from horizontal correspond with deviations from $\theta = \frac{\pi}{2}$.

Figure 1(b) shows a typical trajectory which reveals quasi-periodic orbits in particle orientation. Seen from above [Fig. 1(c)], the trajectory forms a quasi-periodic orbit with lobes similar to those made by a spirograph toy. In the space of tilt (θ) and spin (ψ) shown in Fig. 1(d), it appears to be a simple closed periodic orbit. The mechanism for these tilt-spin orbits is that a tilted ribbon drifts horizontally and begins to spin. The spinning changes which end of the ribbon experiences greater drag and so the tilt changes.

Figure 2 shows many trajectories measured with different initial orientations for each of the four particles. From these data, the six unknown eigenvalues of \mathfrak{a} and \mathfrak{b} can be determined using least-squares fitting of the experimental position and orientation data to trajectories numerically integrated using Eqs. 2. The black lines in Fig. 2 show simulated trajectories using best fit mobility tensors. We see that theory and experiment agree quite well. There are some differences, likely the result of imperfect particle geometry, foreign objects such as lint or bubbles attached to the particles, or systematic orientation measurement errors.

For all four particles, and for all measured initial orientations, the trajectories appear to follow closed orbits in the θ - ψ -plane. Two fixed points, one a center and the other a saddle, appear in each phase diagram. A surprising feature of Fig. 2 is that as the particle increases length from Fig. 2(c) to 2(d), there is a bifurcation at which the fixed points switch stability.

To study the bifurcation as a function of ribbon length, Eqs 2 can be used to obtain evolution equations for the Euler angles. For our co-centered particles, we can use the reference frame in which \mathfrak{a} and \mathfrak{b} are both diagonal to obtain

$$\dot{\psi} = [(b_{11} - b_{22}) \cos^2 \psi - b_{11} + b_{33}] \cos \theta, \quad (3a)$$

$$\dot{\theta} = (b_{11} - b_{22}) \sin \psi \cos \psi \sin \theta, \quad (3b)$$

$$\dot{\phi} = -(b_{11} - b_{22}) \cos^2 \psi + b_{11}. \quad (3c)$$

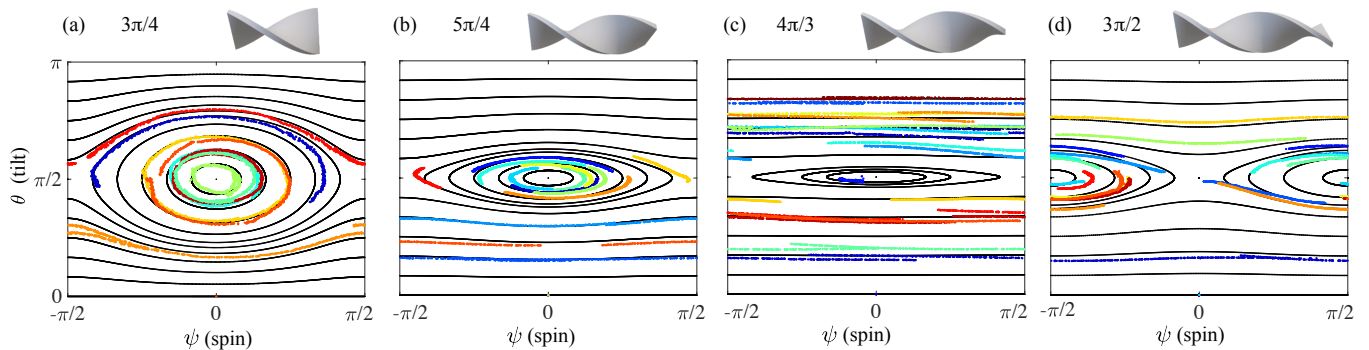


FIG. 2. Angular dynamics for different particle lengths, $2\pi L/s$: (a) $3\pi/4$, (b) $5\pi/4$, (c) $4\pi/3$, and (d) $3\pi/2$. Particle images are above each plot. Solid black lines show numerically integrated trajectories. Color symbols indicate distinct experimental trajectories.

Here the dynamics of the spin angle, $\dot{\psi}$, and the tilt angle, $\dot{\theta}$, do not depend on the azimuthal angle ϕ because there is continuous rotational symmetry about the gravity direction. The continuous translational symmetry in space ensures that the angular dynamics does not depend on the position of the particle center, and so the phase space is two dimensional.

Eqs. 3 show that the angular dynamics changes as $b_{11} - b_{22}$ switches sign, because $\dot{\theta}$ vanishes at this point. Linear stability analysis of Eqs. 3 confirms that for $b_{11} - b_{22} > 0$, the fixed point at $\psi = 0, \theta = \pi/2$ is a center while the fixed point at $\psi = \pi/2, \theta = \pi/2$ is a saddle, and they switch when $b_{11} - b_{22}$ changes sign. Helicoids with $b_{11} = b_{22}$ have axisymmetric translation-rotation coupling and are apparently special particles with simpler dynamics than the general helical ribbon.

Eqs. 3 have a constant of motion [5]. It can be obtained by integrating $d\theta/d\psi = \dot{\theta}/\dot{\psi}$:

$$C = [b_{33} - b_{11} + (b_{11} - b_{22}) \cos^2 \psi] \sin^2 \theta. \quad (4)$$

This constant of motion, C , exists because the dynamics are reversible [27–30], invariant under joint application of time reversal and a reflection in phase space. One way to see reversibility mathematically is that Eqs. 3 are invariant under $t \rightarrow -t$ and $\psi \rightarrow -\psi$. The separate symmetry under $t \rightarrow -t$ and $\theta - \pi/2 \rightarrow \pi/2 - \theta$ would also be sufficient to ensure reversibility. Physically, reversibility can be seen as a consequence of co-centered chiral geometry. A reflection of the particle in space aligned with principal axes, such as $\hat{e}_3 \rightarrow -\hat{e}_3$, converts a helical ribbon from right handed to left handed and switches the signs of the diagonal elements of \mathbb{b} . Combined with time reversal, this also leaves Eqs. (3) invariant. Although the angular dynamics in Eqs. (3) do not conserve phase-space volume, reversibility excludes stable or unstable spiral fixed points and limit cycles.

Note that the second argument above using the physical reflection ensures closed orbits for co-centered chiral particles, but it does not predict closed orbits for par-

ticles with anti-symmetric parts of \mathbb{b} since they do not switch sign in general under spatial reflections. Many chiral particles will have anti-symmetric parts of \mathbb{b} which can cause spiral orbits in orientation space that converge to special orientations given by the eigenvectors of \mathbb{b} [5]. A different case with closed orientation orbits for non-chiral particles was discovered by Miara *et al* [9]. In this case, there is also a symmetry in phase space under reflection and time-reversal.

To understand the possible mobility tensors for helical ribbons, we computed the mobility tensors numerically for ribbons made out of small hydrodynamically interacting spheres that are rigidly connected to each other [8, 31]. The computed mobility tensor eigenvalues for both \mathbb{a} and \mathbb{b} are shown in Fig. 3 as functions of helical ribbon length. Fig. 3(a) shows that the normalized \mathbb{a} eigenvalues change little with length, except at very short lengths where the ribbon becomes more like a thin flat rectangle. The key is in the eigenvalues of \mathbb{b}

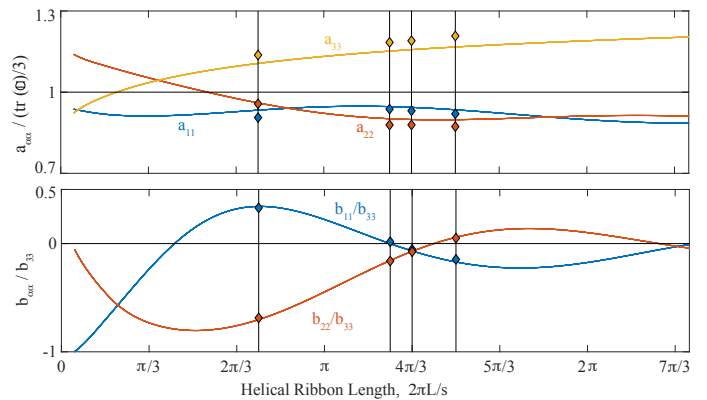


FIG. 3. Diagonal elements of the mobility tensors for \mathbb{a} (top) and \mathbb{b} (bottom) as functions of helical ribbon length. Diamonds indicate experimentally measured values. Solid lines are numerical simulations using the bead-model described in the text.

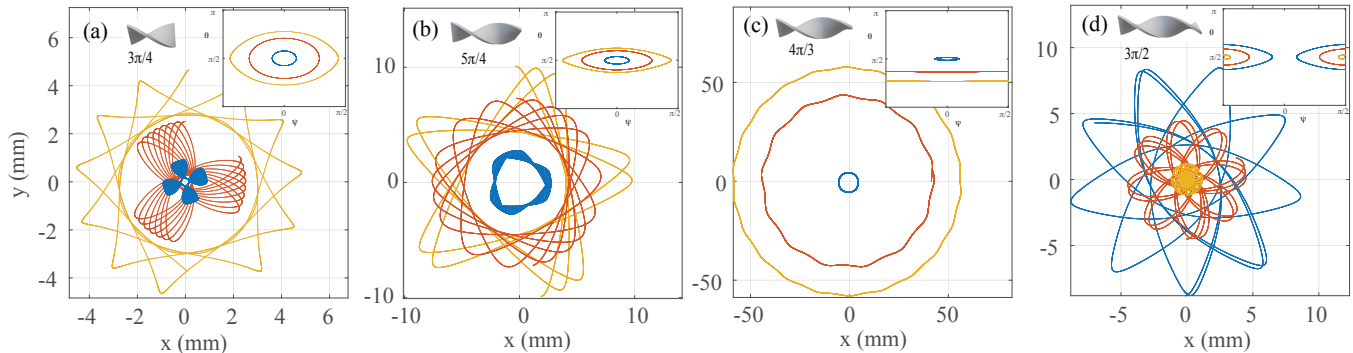


FIG. 4. Spatial trajectories from numerical simulations for selected initial conditions. Insets show the same trajectories (matched by color) in tilt-spin phase space. Helical ribbons lengths are (a) $3\pi/4$, (b) $5\pi/4$, (c) $4\pi/3$, and (d) $3\pi/2$. Videos showing the full range of trajectories are available [24].

shown in Fig. 3(b). Here the critical bifurcation lengths at which $b_{11} = b_{22}$ are clearly shown. In addition to the bifurcation just above $4\pi/3$ seen in Fig. 2, the numerical results show that there are two further bifurcations, near lengths 0.7 and 7.2. There is no apparent special geometric symmetry for particles with any of these lengths. We expect the oscillation to continue as ribbons become longer and approach the simple chiral rod with only b_{33} non-zero.

Figure 3 also shows the experimentally measured eigenvalues of the \mathfrak{a} and \mathfrak{b} tensors. As normalized, the measurements are in quite good agreement with the computed values. We choose to normalize the elements of \mathfrak{a} by its trace and \mathfrak{b} by b_{33} . Discussion of this normalization convention and plots of $\text{Tr } \mathfrak{a}$ and b_{33} are in the supplemental material [24]. In Fig. 3, the deviations between experiment and theory are slightly larger for \mathfrak{a} . This may be a tank-size effect as confinement should especially decrease the measured a_{11} and a_{22} , and the normalization could produce the observed discrepancy [32].

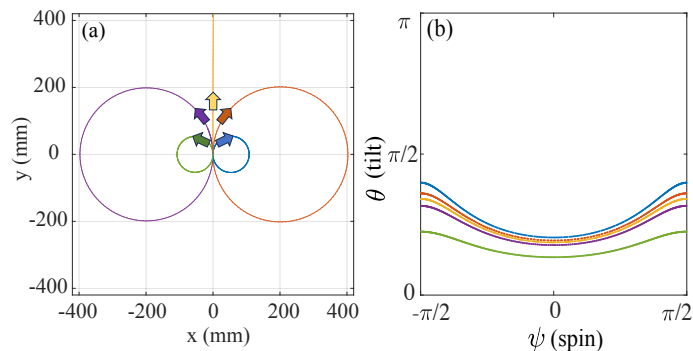


FIG. 5. (a) Spatial trajectory curvature switching for a $3\pi/4$ particle. Arrows indicate direction on the super-helical paths. Trajectories switch from clockwise to counterclockwise as the initial orientation is changed. (b) Phase space orbits of the trajectories in (a), matched by color.

We note that there is some dependence of the numerically simulated mobility tensors on the number and size of the spheres used to represent the helical ribbon. This dependence is negligible for the normalized eigenvalues, but the values of $\text{Tr } \mathfrak{a}$ and b_{33} depend on the detailed configuration of spheres.

The spatial trajectories produced by non-trivial \mathfrak{b} tensors can be very intricate [9]. Orbits in θ - ψ phase space combine with precession in ϕ and the unequal eigenvalues of \mathfrak{a} to produce motion at multiple frequencies. Fig. 4 shows spatial trajectories obtained numerically using fitted mobility tensor values. Experimental trajectories are much shorter, but show the same structure. Trajectories that do not pass through $\theta = \frac{\pi}{2}$ (horizontal) remain tilted [Fig. 4(c)] and have large super-helical spatial trajectories. Those that pass through $\theta = \frac{\pi}{2}$ have complex trajectories similar to those made by the spirograph toy [Figs. 4(a,b,d)]. All four particles show both types, but we only show tilted trajectories in Fig. 4(c).

For some helical ribbons, an interesting phenomenon can occur where the handedness of the spatial trajectory switches signs, shown in Fig. 5. In these cases there exists a critical trajectory for which the helical ribbon is not constrained within a finite horizontal area, in contrast to previous work [33]. This phenomenon can occur when b_{11} and b_{22} have different signs, highlighting the fact that no single number can quantify a particle's chirality; instead, at least a second rank tensor is needed [34]. The \mathfrak{b} tensors measured here provide a useful general tool for quantifying the chirality of a shape.

In conclusion, the helical ribbon is a chiral shape with 3 rotational symmetries that fix the centers of mass, buoyancy, mobility, and resistance to a single point. We find that helical ribbons exhibit strong translation-rotation coupling and identify them as a needed reference case with which more complex particles can be compared. With precise 3-dimensional measurements of position and orientation of helical ribbons sedimenting at particle Reynolds number less than 0.1, we measure both mobil-

ity tensors \mathfrak{a} and \mathfrak{b} . We observe angular orbits that are closed in the two-dimensional space of tilt and spin.

There are helical ribbons with special lengths that have axisymmetric translation-rotation coupling. At these lengths, a bifurcation occurs where the fixed points in tilt-spin space switch between centers and saddles. These axisymmetric helicoids have a particularly simple \mathfrak{b} tensor and can function as a first step on the roadmap that extends to general helical ribbons with triaxial \mathfrak{b} and on to yet more general shapes that are not co-centered. We also find that helical ribbons with b_{11} and b_{22} of opposite signs can have trajectories whose horizontal center-of-mass displacement is unbounded.

Experiments that precisely fabricate complex shapes and measure full mobility tensors have now revealed several unexpected features of translation-rotation coupling during sedimentation [8, 9]. Together with the present work, these point to an important design challenge to create geometries that optimize translation-rotation coupling. Some progress in this direction has been made [35], but the challenge goes far beyond optimizing propulsion efficiency in one dimension. For co-centered particles, each eigenvalue of \mathfrak{b} can be optimized relative to the others to achieve different goals. A full picture of which geometries optimize translation-rotation coupling in Stokes flow could be a major step toward the broader goal of developing better ways to quantify chiral geometry.

SUPPLEMENTAL MATERIAL

Reconstruction of 3D Trajectories

We use three Phantom VEO 640 cameras with nearly orthogonal viewing angles to capture 3D dynamics. LED panels provide bright field illumination onto which black helical ribbons produce clean images. We use methods of camera calibration and orientation measurement developed in [25].

Initial camera calibration parameters are obtained using a static two-plane calibration and then they are refined to sub-pixel accuracy with a dynamic calibration using images of small settling metal spheres.

To find the position and orientation of the helical ribbon from video images, we project a set of points on the surface of an ideal 3D helical ribbon onto the image planes of the three cameras using the camera calibration. The average distance of each these points from a bright pixel in the thresholded image is minimized to find the 3 position and 3 orientation coordinates.

Fabricating Co-Centered Particles

We tried three different methods for fabricating helical ribbons. The first was mechanical twisting of polystyrene

strips. Strips were cut on a paper cutter, twisted with a mechanical jig, annealed at 90° C, and then cut to the desired length. This produced cost effective helical ribbons with variability in width, length, and pitch that required optical sorting to select specific particles. There were also problems with non-reproducible sedimentation dynamics, likely a result of the thin polystyrene having mobility tensors that are very sensitive to tiny imperfections, lint, or bubbles.

The second method was 3D printing with a Form2 printer from Formlabs. This produced reproducible trajectories, but there was a measurable offset of the steady sedimentation orientation which we believe is due to density inhomogeneity in the printed material. This method also has some challenges because it prints a single material and so supports must be removed by hand introducing some shape irregularities.

We then obtained particles 3D printed with projection micro stereolithography developed by Boston Micro Fabrication whose equilibrium sedimentation orientation matches the expectations from the symmetry of the particles. Their primary drawback is the higher cost per particle.

We have come to view Stokes sedimentation dynamics as one of the most sensitive tools available for detecting irregularities in geometry or mass density of rigid bodies.

Mobility tensor normalization

We measure diagonal elements of the \mathfrak{a} and \mathfrak{b} mobility tensors and normalize them by $\text{tr}(\mathfrak{a})/3$ and b_{33} respectively. Physically, $\text{tr}(\mathfrak{a})/3$ is the average drag over all orientations. However, $\text{tr}(\mathfrak{b})$ can be zero, so this is not a good normalization for \mathfrak{b} . Instead, for this particle we choose to normalize by b_{33} , because it is larger than the other two eigenvalues and its sign is preserved as we change the helical ribbon length. In the limit of infinite length, b_{33} is the only non-zero eigenvalue.

Figure 6 provides absolute scaling values of the normalization factors used for \mathfrak{a} and \mathfrak{b} . Notably, the helical ribbon’s mass increases faster than its drag as length increases, resulting in smaller sedimentation velocities for shorter particles.

Movies of spatial trajectories

The spatial trajectories of an arbitrary particle fall in a hierarchy of complexity governed by the number of distinct \mathfrak{a} and \mathfrak{b} eigenvalues. \mathfrak{b} determines what frequencies are present and \mathfrak{a} determines if those frequencies can couple to spatial dynamics.

To communicate the wide range of spatial trajectories that are possible, we created movies showing how the trajectories change as the initial orientation

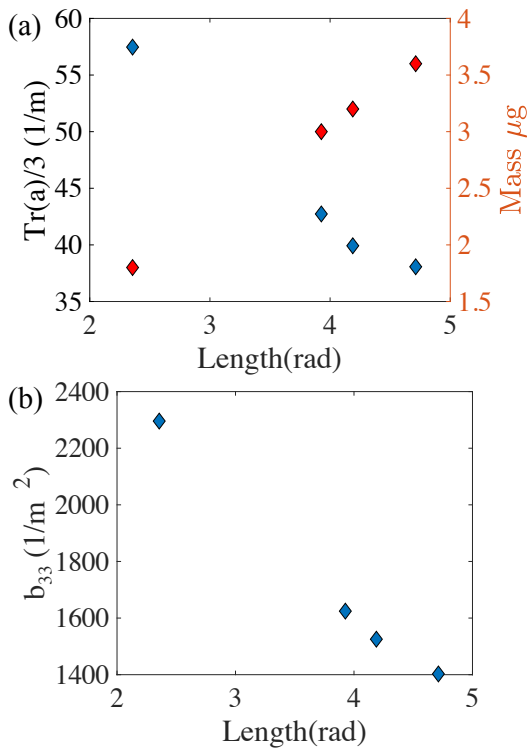


FIG. 6. Normalization factors for mobility tensors as a function of helical ribbon length. (a) Average of the eigenvalues of \mathbf{a} (b) Largest eigenvalue of \mathbf{b} .

is continuously changed. Movies are available at: <https://www.youtube.com/channel/UCVrg1jeDOSidH7oYnLdqZ2Q>. The movies show simulated trajectories using mobility tensors measured with fits to experimental data for each of the four helical ribbon lengths that we measured. The shortest and longest particles show switching of the handedness of spatial trajectories because the values of b_{11} and b_{22} (shown in Fig. 3 in the main article) have opposite signs. This allows cancellation of contributions to the change in ϕ along the trajectory. The other two particles always have left handed trajectories because the negative eigenvalues dominate.

Additionally, a video of the example trajectory shown in Fig. 1 is available at: <https://www.youtube.com/watch?v=n9FWTLHiUK4>. The angular phase space is pictured at the bottom left with the same axes as in Fig. 1(d).

We thank Bennet Grossman for assistance in setting up the experimental apparatus and Gleb Shevchuk for conversations about advanced 3D printing techniques. We acknowledge support from the NSF under grant DMR-1508575 and CBET-2211704, the Army Research Office under grant W911NF-17-1-0176, and Vetenskapsrådet under grant no. 2021-4452.

* gvoth@wesleyan.edu

- [1] J. S. Guasto, R. Rusconi, and R. Stocker, *Annual Review of Fluid Mechanics* **44**, 373 (2012).
- [2] B. R. Sutherland, M. DiBenedetto, A. Kaminski, and T. van den Bremer, *Phys. Rev. Fluids* **8**, 070701 (2023).
- [3] J. Happel and H. Brenner, *Low Reynolds number hydrodynamics: with special applications to particulate media*, Vol. 1 (Springer Science & Business Media, 1983).
- [4] S. Kim and S. J. Karrila, *Microhydrodynamics: principles and selected applications* (Butterworth-Heinemann, Boston, 1991).
- [5] T. A. Witten and H. Diamant, *Reports on progress in physics* **83**, 116601 (2020).
- [6] E. M. Purcell, *Proceedings of the National Academy of Sciences* **94**, 11307 (1997).
- [7] E. J. Tozzi, C. T. Scott, D. Vahey, and D. J. Klingenberg, *Physics of Fluids* **23**, 033301 (2011).
- [8] D. Collins, R. J. Hamati, F. Candelier, K. Gustavsson, B. Mehlig, and G. A. Voth, *Physical Review Fluids* **6**, 074302 (2021).
- [9] T. Miara, C. Vaquero-Stainer, D. Pihler-Puzović, M. Heil, and A. Juel, *Communications Physics* **7**, 47 (2024).
- [10] F. Djutanta, P. T. Brown, B. Nainggolan, A. Coullomb, S. Radhakrishnan, J. Sentosa, B. Yurke, R. F. Hariadi, and D. P. Shepherd, *Proceedings of the National Academy of Sciences* **120**, e2220033120 (2023).
- [11] L. Kelvin, *Phil. Mag.* **42**, 362 (1871).
- [12] K. Gustavsson and L. Biferale, *Phys. Rev. Fluids* **1**, 054201 (2016).
- [13] O. Gonzalez, A. Graf, and J. Maddocks, *Journal of Fluid Mechanics* **519**, 133 (2004).
- [14] M. Doi and M. Makino, *Physics of Fluids* **17**, 043601 (2005).
- [15] N. W. Krapf, T. A. Witten, and N. C. Keim, *Physical Review E* **79**, 056307 (2009).
- [16] M. Palusa, J. De Graaf, A. Brown, and A. Morozov, *Physical Review Fluids* **3**, 124301 (2018).
- [17] B. Moths and T. A. Witten, *Phys. Rev. E* **88**, 022307 (2013).
- [18] F. Bretherton, *J. Fluid Mech.* **14**, 284 (1962).
- [19] J. Fries, J. Einarsson, and B. Mehlig, *Phys. Fluids* **2**, 014302 (2017).
- [20] K. Ishimoto, *Journal of Fluid Mechanics* **892**, A11 (2020).
- [21] K. Ishimoto, *Physics of Fluids* **32**, 081904 (2020).
- [22] M. Kim, J. C. Bird, A. J. Van Parys, K. S. Breuer, and T. R. Powers, *Proceedings of the National Academy of Sciences* **100**, 15481 (2003).
- [23] B. Rodenborn, C.-H. Chen, H. L. Swinney, B. Liu, and H. P. Zhang, *Proceedings of the National Academy of Sciences* **110** (2013).
- [24] "Supplementary material."
- [25] T. B. Oehmke, A. D. Bordoloi, E. Variano, and G. Verhille, *Physical Review Fluids* **6**, 044610 (2021).
- [26] H. Goldstein, *Classical Mechanics* (Addison-Wesley, 1980).
- [27] V. I. Arnold, in *Nonlinear and Turbulent Processes in Physics* (1984) p. 1161.
- [28] S. H. Strogatz, *Nonlinear dynamics and Chaos* (Westview Press, 1994).

- [29] A. Politi, G. L. Oppo, and R. Badii, *Phys. Rev. A* **33**, 4055 (1986).
- [30] J. Einarsson, B. M. Mihiretie, A. Laas, S. Ankardal, J. R. Angilella, D. Hanstorp, and B. Mehlig, *Physics of Fluids* **28**, 013302 (2016).
- [31] L. Durlinsky, J. F. Brady, and G. Bossis, *J. Fluid Mech.* **195**, 257 (1988).
- [32] A. Roy, R. J. Hamati, L. Tierney, D. L. Koch, and G. A. Voth, *J. Fluid Mech.* **875**, 576 (2019).
- [33] M. Makino *et al.*, *Physics of Fluids* **17** (2005).
- [34] E. Efrati and W. T. M. Irvine, *Physical Review X* **4**, 011003 (2014).
- [35] E. E. Keaveny, S. W. Walker, and M. J. Shelley, *Nano Letters* **13**, 531 (2013).